





# Multiple Emission Regions in Jets of the Low-Luminosity Active Galactic Nucleus in NGC 4278

Samik Dutta<sup>1,2</sup>  and Nayantara Gupta<sup>3</sup> <sup>1</sup> University of Calcutta, 92 Acharya Prafulla Chandra Road, Rajabazar, Kolkata, West Bengal 700009, India; [samikduttaphy@gmail.com](mailto:samikduttaphy@gmail.com)<sup>2</sup> Birla Institute of Technology and Science—Pilani, Vidya Vihar, Pilani, Rajasthan 333031, India<sup>3</sup> Raman Research Institute, C. V. Raman Avenue, 5th Cross Road, Sadashivanagar, Bengaluru, Karnataka 560080, India; [nayan@rri.res.in](mailto:nayan@rri.res.in)

Received 2024 March 28; revised 2024 August 6; accepted 2024 August 7; published 2024 October 4

## Abstract

The Large High Altitude Air Shower Observatory (LHAASO) has detected very-high-energy gamma rays from the low-ionization nuclear emission-line region galaxy NGC 4278, which has a low-luminosity active galactic nucleus (LLAGN) and symmetric, mildly relativistic S-shaped twin jets detected by radio observations. Few LLAGNs have been detected in gamma rays due to their faintness. Earlier, several radio-emitting components were detected in the jets of NGC 4278. We model their radio emission with synchrotron emission of ultra-relativistic electrons to estimate the strength of the magnetic field inside these components within a time-dependent framework after including the ages of the different components. We show that the synchrotron and synchrotron self-Compton emission by these components cannot explain the Swift X-ray data and the LHAASO gamma-ray data from NGC 4278. We suggest that a separate component in one of the jets is responsible for the high-energy emission, whose age, size, magnetic field, and the spectrum of the ultra-relativistic electrons inside it have been estimated after fitting the multiwavelength data of NGC 4278 with the sum of the spectral energy distributions from the radio components and the high-energy component. We note that the radio components of NGC 4278 are larger than the high-energy component, which has also been observed in several high-luminosity active galactic nuclei.

*Unified Astronomy Thesaurus concepts:* [Gamma-rays \(637\)](#); [Low-luminosity active galactic nuclei \(2033\)](#); [Galaxy jets \(601\)](#)

## 1. Introduction

Low-ionization nuclear emission-line regions (LINERs), first identified as a class of galaxies more than 40 yr ago (T. M. Heckman 1980), are the most abundant population of active galactic nuclei (AGNs) in our neighborhood. The study of such LINER galaxies could bridge our knowledge and understanding between normal and active galaxies (I. Márquez et al. 2017). The sources of this subclass of AGNs are identified by their low-ionization, narrow emission lines from gas ionized by a nonstellar source (H. Netzer 2015). Due to their low accretion rate, they are faint and thus less often detected, although they are abundant in nearby galaxies. Around 40% of galaxies in the Palomar Spectroscopic Survey are AGNs, including LINER galaxies, Seyfert nuclei, and transition objects (L. C. Ho et al. 1997a).  $H\alpha$  components are detected in a large number of LINERs, and in many cases points like X-ray or UV sources are also detectable at their nuclei; these LINERs are known as LINER 1.9s (L. C. Ho et al. 1997b), and they form a subclass of low-luminosity AGNs (LLAGNs). Their average bolometric luminosity is less than  $10^{42}$  erg  $s^{-1}$  (Y. Terashima et al. 2000). It is also important to note that the commonly observed “big blue bump” from the standard accretion disk in more luminous AGNs is either absent or weak in LLAGNs (L. C. Ho 2008).

Previously, many LLAGNs have been described by advection-dominated accretion flows (ADAFs), which are radiatively inefficient for sub-Eddington accretion rates with low densities and low optical depths. This results in a

geometrically thick and optically thin accretion flow, unlike the geometrically thin and optically thick accretion flows in luminous AGNs (R. Narayan & I. Yi 1994). An optically thin ADAF is usually referred to as a radiatively inefficient accretion flow (RIAF). The emission in LLAGNs may come from the jet, the RIAF, and the outer thin disk (R. S. Nemmen et al. 2014). Their relative contribution may vary from one source to another. R. S. Nemmen & M. S. Brotherton (2010) modeled 24 LINERs, and showed that both an ADAF model and a jet model can explain the observed X-ray data.

It is not known how similar LLAGNs are to more luminous AGNs. GeV energy gamma rays have been detected by Fermi-LAT from NGC 315, NGC 4261, NGC 1275, and NGC 4486 (R. de Menezes et al. 2020). Multiwavelength data analysis and modeling suggest that single-zone synchrotron self-Compton (SSC) emission from the jet can explain the gamma-ray emission up to a few GeV from NGC 315 and NGC 4261, while hadronic emission from a RIAF cannot explain the gamma-ray data. These sources were further studied (G. Tomar et al. 2021), and the authors reported that SSC emission from a subparsec-scale jet can explain the gamma-ray data from all these four LLAGNs; however, external Compton emission from kiloparsec-scale jets of NGC 315 and NGC 4261 is needed to explain the gamma-ray data beyond 1.6 GeV and 0.6 GeV, respectively. In a more recent paper (G. Tomar & N. Gupta 2023), a detailed multiwavelength study of the nearby LLAGN M81\* was carried out at different quiescent and flaring states. The radio and X-ray data of different epochs are well fitted by synchrotron emission of ultra-relativistic electrons, and the authors found this source has a similarity with high-synchrotron peaked blazars. A comparison of the characteristics of the LLAGN NGC 4278 to BL Lac objects, Seyfert

galaxies, and LINERs was discussed in the paper by J.-S. Lian et al. (2024).

NGC 4278 is an elliptical galaxy located at a distance of 16.4 Mpc (J. L. Tonry et al. 2001). L. C. Ho et al. (1997b) classified this source as a LINER 1.9 by confirming the presence of a broad  $H\alpha$  line with an energy flux of  $\log F(H\alpha) = -13.07$  erg cm<sup>-2</sup> s<sup>-1</sup>; hence, it is a LLAGN. The mass of its black hole is  $3.09 \pm 0.58 \times 10^8 M_\odot$  (T.-G. Wang & X.-G. Zhang 2003; M. Chiaberge et al. 2005), which implies an Eddington luminosity of  $3.9 \times 10^{46}$  erg s<sup>-1</sup>. G. Younes et al. (2010) carried out simultaneous and quasi-simultaneous X-ray and multiwavelength study of this source and pointed out that, at a low X-ray flux, the spectral energy distribution (SED) of NGC 4278 is similar to that of a typical LINER source where the radio to X-ray emission can be considered as originating from a jet and/or a RIAF. In contrast, at a high state of X-ray emission, it is more like a low-luminosity Seyfert. Hence, they concluded that NGC 4278 may appear as a LINER or a Seyfert depending on the intensity of its X-ray emission.

M. Giroletti et al. (2005) reported a detailed study of the radio-emitting components in the jets of NGC 4278 using observational data from the Very Long Baseline Array (VLBA) at 5 and 8.4 GHz. Their analysis revealed a two-sided structure, with symmetric S-shaped jets emerging from a flat-spectrum core. Assuming that the radio morphology is intrinsically symmetric and Doppler beaming effects govern its appearance, they found that NGC 4278 has mildly relativistic jets ( $\beta \sim 0.75$ ), one of which is closely aligned to the line of sight ( $2^\circ \leq \theta \leq 4^\circ$ ). An alternative scenario suggested in their paper is the source could be oriented at a larger angle and asymmetries could be related to the jets' interaction with the surrounding medium. The details of the radio observations from their paper are discussed in the next section. We have used the radio data recorded by the VLBA in 2000 from the four components S1, S2, N3, and N2 in the jets of NGC 4278 and fitted their radio flux at 5 and 8.4 GHz with synchrotron emission of ultra-relativistic electrons to estimate the magnetic fields inside these components within a time-dependent framework, where the electron spectra evolved with time. M. Giroletti et al. (2005) provides the Doppler factor of the jet frame, the sizes of the radio components, and their ages in the year 2000, which we have used to determine their multi-wavelength SEDs with the SSC model.

NGC 4278 has also been observed in X-ray by Swift-XRT and in gamma-ray energy bands by AGILE and Fermi-LAT (L. Baldini et al. 2021; Z.-R. Wang et al. 2024).<sup>4,5</sup> The Large High Altitude Air Shower Observatory (LHAASO) has also reported very-high-energy gamma-ray detection from a source, 1LHAASO J1219+2915, which is located at a distance of  $0.05^\circ$  from NGC 4278 (Z. Cao et al. 2024b).<sup>6</sup> More recently, they have reported that the TeV source is located within  $0.03^\circ$  of NGC 4278 (Z. Cao 2024a). Observations by LHAASO's Water Cherenkov Detector Array (WCDA) during the active period have a significance of  $8.8\sigma$ . In AGN studies, identifying the region of emission in different frequencies is crucial to understanding the underlying mechanisms of jet emission. Sometimes correlation is found between emissions in different frequencies, which helps us to unveil the populations of electrons responsible for the emissions and model the sources

in detail. The low-luminosity AGN population remains unexplored in comparison to the high-energy one. It is important to know which component in the jets of NGC 4278 could be responsible for the high-energy emission to understand the characteristics of this class of AGN. We have modeled the multiwavelength data of NGC 4278 to identify a possible emission region of the X-rays and gamma rays in one of the mildly relativistic jets.

## 2. Radio Observation of Components in Jets of NGC 4278

NGC 4278 was observed with an 11-element very-long-baseline interferometry array made up of the NRAO's VLBA on 2000 August 27. The observations were conducted by switching between 5 and 8.4 GHz. The initial calibration was performed by the NRAO Astronomical Image Processing System (AIPS), and similar data-reduction techniques were followed for both 5 and 8.4 GHz data sets.

M. Giroletti et al. (2005) revealed that NGC 4278 is dominated by a compact component ‘‘C’’ ( $T_B = 1.5 \times 10^9$  K) at the center with jets on either side of it. In the southeast, the jet extends for  $\sim 6.5$  mas before turning east. This jet-like feature is 20 mas which corresponds to  $\sim 1.4$  pc long. On the other side, the jet-like feature is elongated to the north in the 5 GHz map, and the 8.4 GHz map also clearly shows a secondary component. Finally, this northern jet-like feature turns into a diffuse, low-brightness region as it bends to the west. NGC 4278 extends over  $\sim 45$  mas, which corresponds to about 3 pc. It is classified as a compact symmetric object (CSO), except that it is underluminous when compared to most known CSOs (A. B. Peck & G. B. Taylor 2000). A total flux density of 120 mJy at 5 GHz and 95 mJy at 8.4 GHz is measured. This visibility data is fitted by a five-component model at both of these frequencies. The sizes of the jet emission regions and their flux densities at 5 and 8.4 GHz are calculated from the parameters of the Gaussian component for the model brightness distribution of the fitting.

The jet components S1, S2, N2, and N3 are named based on the most likely epoch of ejection. Information on the evolution of the source is obtained by comparing data taken at the same frequency in different epochs. Reprocessed data from July 1995 (5 GHz) are overlaid with the data from 2000 August (5 GHz) to highlight any change in the source structure. The overall morphology of NGC 4278 is seen to be almost identical to G. Giovannini et al. (2001).

For each component, the radial distance increased over the 5 yr between observations, with larger motions on the north-western side. N2 was displaced the most, with the component moving at  $\sim 0.17c$ . This observation argues that the northern jet is the one pointing toward us. M. Giroletti et al. (2005) found that this jet is oriented close to the line of sight ( $2^\circ \lesssim \theta \lesssim 4^\circ$ ) and has a mildly relativistic velocity of  $\beta \sim 0.76$  with a corresponding Doppler factor  $\delta \sim 2.7$ .

The ages of the components have been derived after assuming a constant apparent velocity for each component of NGC 4278. S2 and N2 are reported to be about 29 and 25 yr old, with S1 being the oldest component (65.8 yr old) and N3 being the youngest (8.3 yr old) in 2000. The ages of the respective components, their sizes, and the Doppler factor  $\delta \sim 2.7$  (for the jet pointing toward us) of the jet frame have been used by us to model their multiwavelength SEDs. We have denoted them as the radio components in Figures 1, 2, 3, and 5. The errors in the radio fluxes are not given in Table 2 of

<sup>4</sup> <http://agile.rm.iasf.cnr.it>

<sup>5</sup> <http://www-glast.stanford.edu>

<sup>6</sup> <http://english.ihep.cas.cn/lhaaso/>

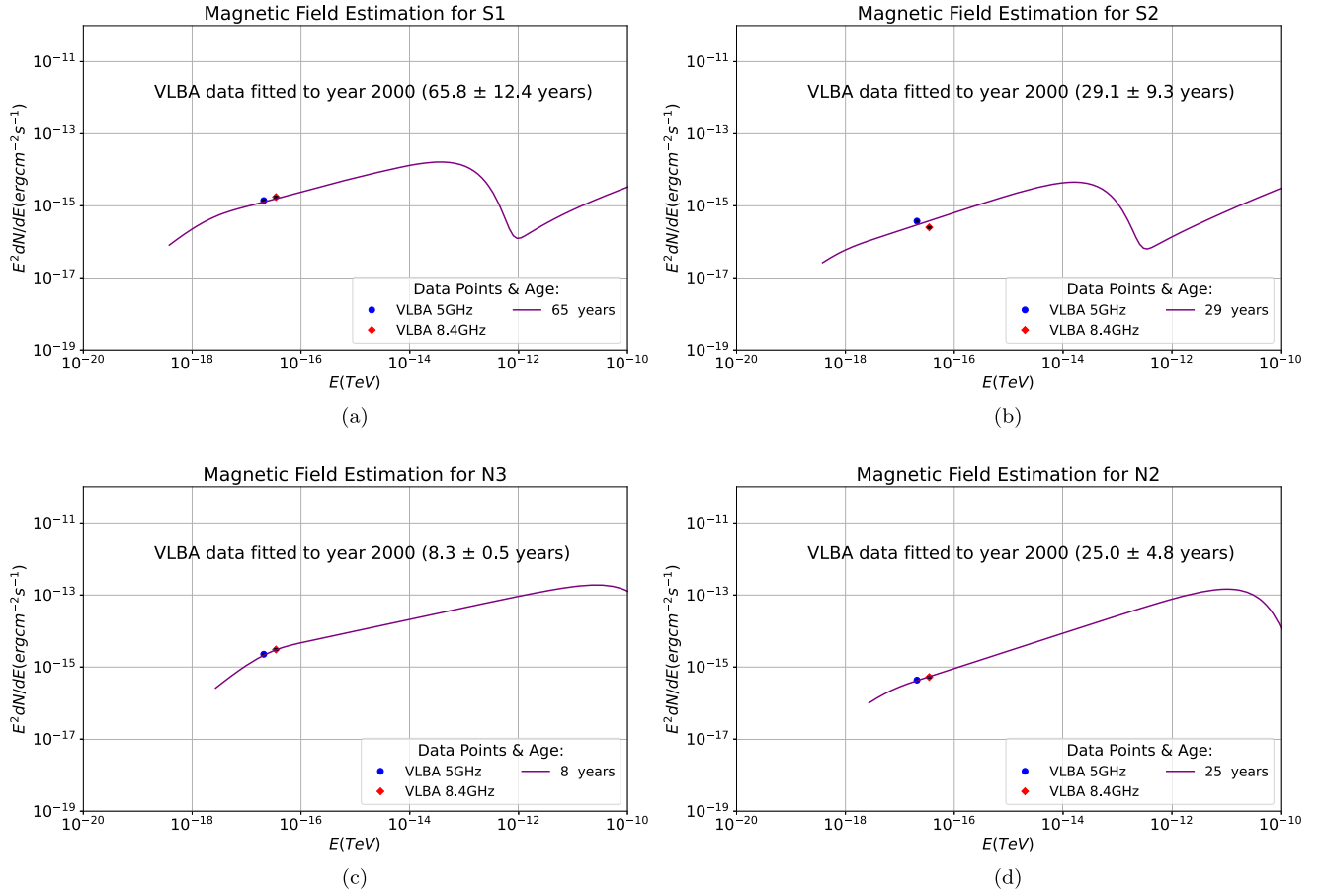


**Figure 1.** Radio data of the year 2000 from the radio components reported in M. Giroletti et al. (2005) have been fitted with synchrotron emission considering the time evolution of the accelerated electron spectra. The ages of the components in the year 2000 are also mentioned. The values of the parameters used to get the radio spectra are given in Table 1 of this paper. Errors on the radio data points are assumed to be 5% following Table 1 of M. Giroletti et al. (2005).

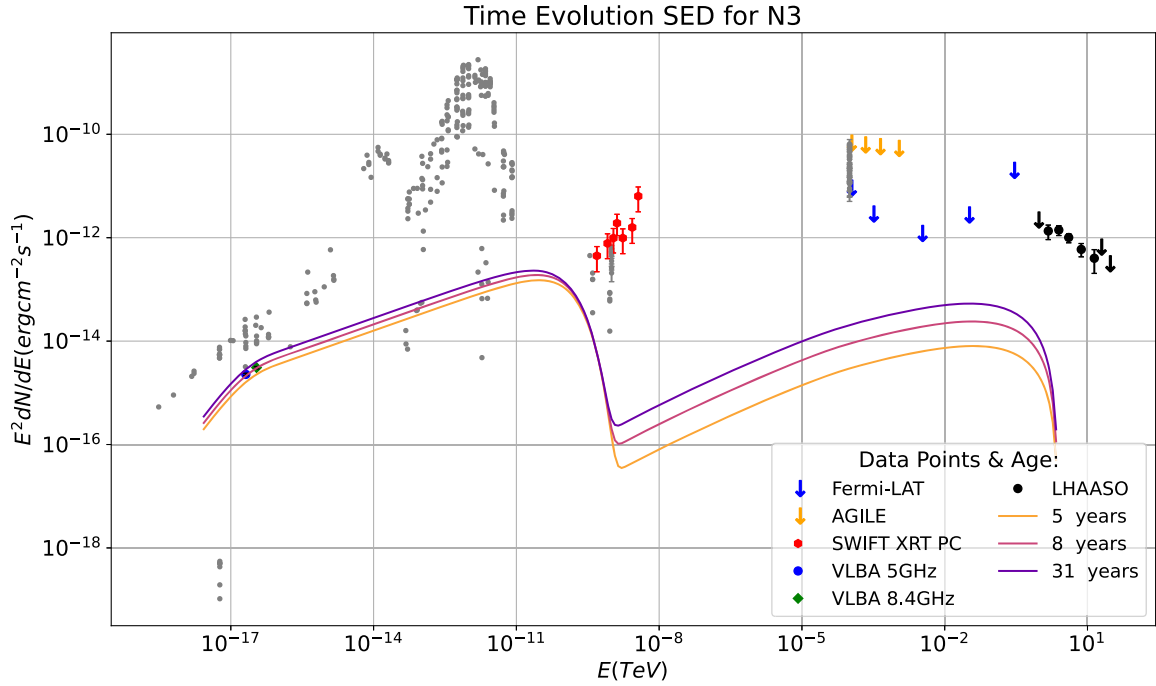


**Figure 2.** The time evolution of the SED of the youngest radio component, N3, shown in the years 2000 and 2023. Swift X-ray data (red solid circles) and Fermi-LAT upper limits (blue downward arrows; Z.-R. Wang et al. 2024) are shown. The black downward arrows and black solid circles represent LHAASO upper limits and data points of NGC 4278 (Z. Cao 2024a). The orange downward arrows represent the AGILE upper limits (A. Bulgarelli et al. 2019). The archival data points (gray solid circles) are from the Energetic Gamma Ray Experiment Telescope (R. C. Hartman et al. 1999), ROSAT All Sky Survey (W. Voges et al. 1999), WGACAT (N. E. White et al. 2000), and NASA/IPAC Extragalactic Database catalogs.

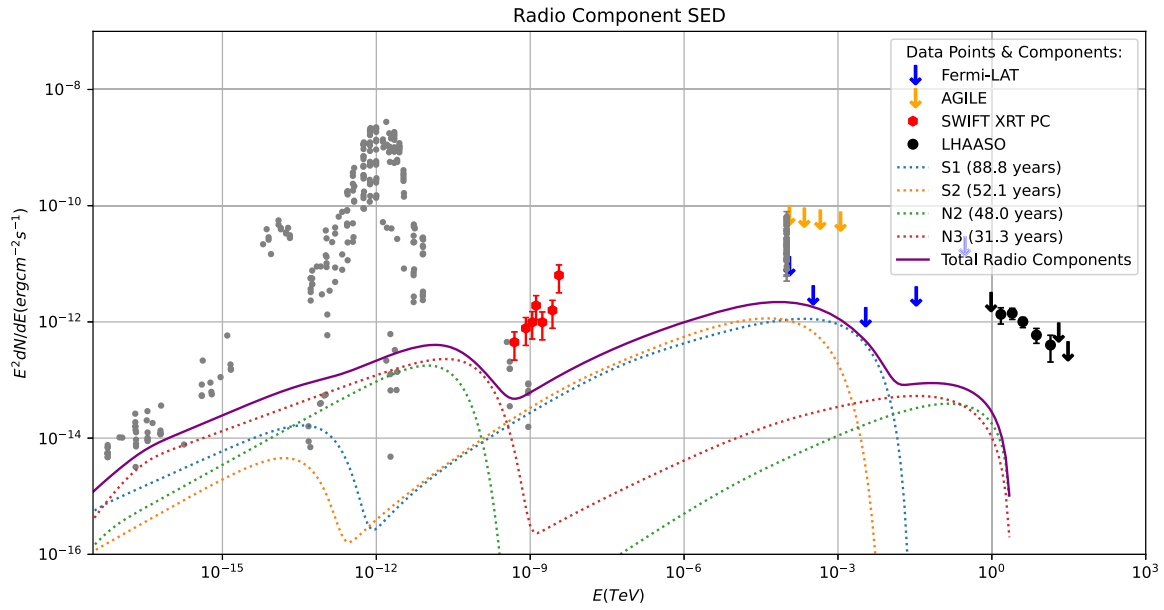


**Figure 3.** SSC model used to obtain the multiwavelength SED from each radio component in the year 2023 (dotted lines); their sum is shown with the solid line and compared with the observational data points as mentioned in Figure 2. The values of the model parameters of the components used to obtain the SEDs are mentioned in Table 1.

**Table 1**

Parameters Used to Fit the Radio Data of the Jet Components of NGC 4278 with a Simple Power-law Form of Injected Electron Spectrum  $Q(E/E_0) \propto \left(\frac{E}{E_0}\right)^{-\alpha}$

Parameters	S2	S1	N3	N2
Power injected in electrons (in $\text{erg s}^{-1}$ )	$7.5 \times 10^{42}$	$1.0 \times 10^{43}$	$2.0 \times 10^{40}$	$2.25 \times 10^{40}$
Reference energy ( $E_0$ in GeV)	$10^3$	$10^3$	$10^3$	$10^3$
Maximum energy of electrons injected ( $E_{\text{max}}$ in GeV)	50	100	$10^3$	$10^3$
Minimum energy of electrons injected ( $E_{\text{min}}$ in GeV)	0.16	0.32	0.32	0.32
Spectral index of injected spectrum ( $\alpha$ )	2.0	2.17	2.35	2.02
Magnetic field in emission region ( $B$ in mG)	0.8	0.55	0.9	0.2
Size of emission region ( $R$ in pc) <sup>a</sup>	0.0748	0.3695	0.18734	0.5398
Escape time ( $t_{\text{esc}}$ in sec)	$10R/c$	$10R/c$	$10R/c$	$10R/c$
Age of component (in 2000 in years) <sup>a</sup>	$29.1 \pm 9.3$	$65.8 \pm 12.4$	$8.3 \pm 0.5$	$25.0 \pm 4.8$
Age of component (in 2023 in years)	52.1	88.8	31.3	48.0
Doppler factor of component ( $\delta$ ) <sup>a</sup>	0.38	0.38	2.7	2.7
Distance to the component (in Mpc) <sup>b</sup>	16.4	16.4	16.4	16.4

**Notes.**

<sup>a</sup> M. Giroletti et al. (2005).

<sup>b</sup> J. L. Tonry et al. (2001).

M. Giroletti et al. (2005). In Table 1, the error in the total flux is about 5%, and based on this information, we have assumed the error in the flux of individual components is 5%, which is not noticeable in our figures.

### 2.1. Modeling the Radio Data from Individual Components

The size and age of the individual components S1, S2, N3, and N2 are given in M. Giroletti et al. (2005), which we have used to calculate the radio spectrum from each of them. We have assumed that electrons are accelerated inside these components to ultra-relativistic energies, and that they lose energy due to synchrotron and SSC emission; as a result of this, the radio spectrum is produced.

The GAMERA code (J. Hahn et al. 2022) has been used to solve the transport equation to generate the time-evolved electron spectrum inside each component. This code also

calculates the resulting radiation spectra. The transport equation for electrons is given by

$$\frac{\partial N}{\partial t} = Q(E, t) - \frac{\partial(bN)}{\partial E} - \frac{N(E, t)}{t_{\text{esc}}}, \quad (1)$$

where  $Q(E, t)$  is the injection spectrum of electrons produced by shock acceleration in an inhomogeneous magnetic field. A shock-accelerated electron spectrum may follow a simple power-law distribution if the electrons are accelerated by the first-order Fermi mechanism:

$$Q(E/E_0) = A \left(\frac{E}{E_0}\right)^{-\alpha}, \quad (2)$$

where the normalization constant  $A$  is determined by the injected luminosity in electrons,  $E_0$  is the reference energy, and

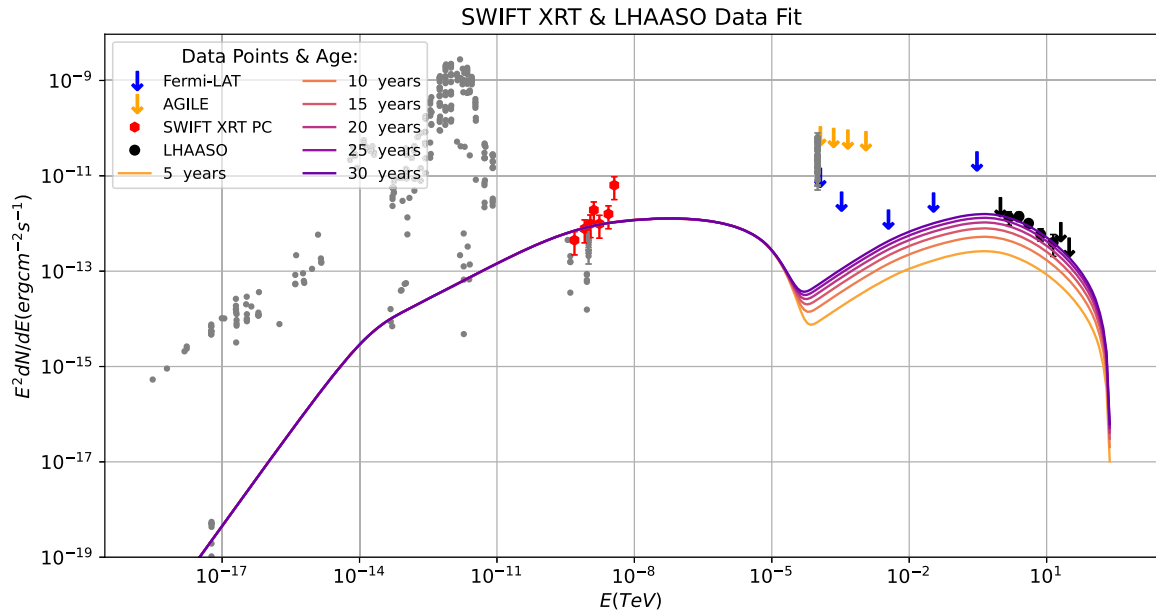


**Figure 4.** High-energy emission from a component in the jet of NGC 4278 pointed towards us in the year 2023 assuming its age is 30 yr, which can explain the Swift X-ray (Z.-R. Wang et al. 2024) and LHAASO gamma-ray data (Z. Cao 2024a). The SSC model is used to obtain the multiwavelength SED. The values of the model parameters used to get this SED are mentioned in Table 2. The time evolution of the SED is also shown.

$\alpha$  is the spectral index. We only have two data points for each radio component, which cannot constrain the spectral shape; however, the shape of the injected spectrum inside the radio components does not affect the result and conclusion of this work. Synchrotron and SSC are the most important energy-loss processes in this case. These energy losses are included in the transport equation given in Equation (1) by the term  $b(E, t)$ .  $t_{\text{esc}}$  denotes the timescale at which the electrons escape from the emission region.  $N(E, t)$  is the resultant electron spectrum at any time  $t$ . The Doppler factor of the jet frame has been used from M. Giroletti et al. (2005). In the first-order Fermi mechanism, the spectral index of the shock-accelerated electrons is close to  $-2$ , which has been used for the radio components. We have varied the magnetic field and the normalization of the electron spectrum to fit the radio data recorded in the year 2000 by the VLBA at 5 and 8.4 GHz from each of the components S1, S2, N3, and N2. The radio spectra and data points are shown in Figure 1. We could not fit the radio data points of the S2 component as the flux measured at 8.4 GHz is lower than that at 5 GHz. Subsequently, the electron spectra inside the components evolved in time until the year 2023, when all the values of the model parameters remained constant except the ages of the radio components. We show the time evolution of the multiwavelength SED from the youngest component, N3, in Figure 2. The multiwavelength SED has not reached a steady state, hence a time-dependent model is needed for NGC 4278. In the years 2000 and 2023, this component was 8 yr and 31 yr old, respectively. The SEDs are extended from radio to gamma-ray energy using the SSC model and added to get the total SED, as shown in Figure 3. The values of the parameters used to obtain the SEDs shown in Figures 1, 2, and 3 are given in Table 1. The data from the year 2000 constrain the values of the parameters of the radio components. The archival radio data points are mostly above all the components' total radio flux.

### 3. Modeling X-Ray and Gamma-Ray Data from NGC 4278

The Swift X-ray and Fermi-LAT data were analyzed by Z.-R. Wang et al. (2024), who obtained some upper limits after reducing the Fermi-LAT data. We have used the Fermi-LAT upper limits and the Swift data points from their paper to compare with our model prediction. LHAASO is a multi-purpose extensive air-shower array. It consists of three interconnected detector arrays, a  $\text{km}^2$  array (KM2A) for gamma-ray detection above 10 TeV, the 78,000  $\text{m}^2$  WCDA for TeV gamma-ray detection, and the Wide Field of View Cherenkov Telescope Array (WFCTA) for cosmic-ray detection. Very-high-energy gamma-ray flux has been recorded using the WCDA by Z. Cao (2024a). The Swift X-ray (Z.-R. Wang et al. 2024) and LHAASO gamma-ray data recorded by the WCDA (Z. Cao 2024a) cannot be fitted after adding the SEDs of the radio components S1, S2, N3, and N2, as shown in Figure 3. We suggest that there is an additional component in the jet which is responsible for the high-energy emission. This high-energy component has a smaller size, and electrons are accelerated to very high energy within it. A power-law injection spectrum of ultra-relativistic electrons in the form of Equation (2) has been adapted to obtain the high-energy photon emission radiated by the electrons. We solve the transport equation of Equation (1) to get the time-evolved electron spectrum after including injection, energy loss, and the escape of electrons; subsequently, the SED is obtained at the current age of the high-energy component. The SED of the synchrotron and SSC emission is shown in Figure 4. After adding the SED of the high-energy component to the SEDs of the radio components, the total SED is shown in Figure 5 and compared with the observational data. The values of the parameters used to fit the high-energy data are listed in Table 2.

### 4. Results

We have fitted the VLBA radio data at 5 and 8.4 GHz of the four components S1, S2, N3, and N2 in Figure 1. The simulated spectra fit the radio data points of the radio

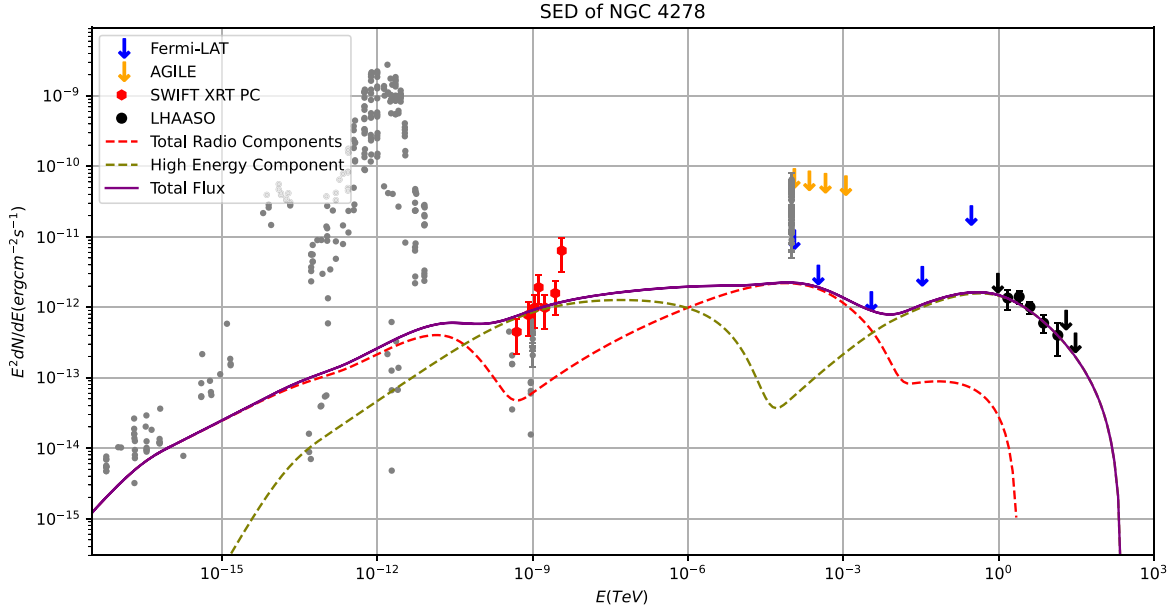


**Figure 5.** The total SED in the year 2023 is calculated after adding the SEDs of the radio components shown in Figure 3 to the SED of the high-energy emission shown in Figure 4. A comparison of our model prediction with multiwavelength observational data is shown.

**Table 2**

Parameters Used to Fit the High-energy Data of NGC 4278 with a Power-law Form of Injected Electron Spectrum  $Q(E/E_0) \propto (E/E_0)^{-\alpha}$

Parameters	High-energy Component
Power injected in electrons (in $\text{erg s}^{-1}$ )	$5 \times 10^{39}$
Reference energy ( $E_0$ in GeV)	$10^3$
Maximum energy of electrons injected ( $E_{\text{max}}$ in GeV)	$10^5$
Minimum energy of electrons injected ( $E_{\text{min}}$ in GeV)	3.16
Spectral index of injected spectrum ( $\alpha$ )	2.0
Magnetic field in emission region (B in mG)	8.0
Size of emission region (R in pc)	0.005
Escape time ( $t_{\text{esc}}$ in sec)	$10R/c$
Age of component (in 2023 in years)	30.0
Doppler factor of component ( $\delta$ )	2.7
Distance to the component (in Mpc) <sup>a</sup>	16.4

**Note.**

<sup>a</sup> J. L. Tonry et al. (2001).

components S1, N2, and N3; only for the S2 component, it is not possible to fit the radio data points. Although we cannot constrain the shape of the radio spectrum, it does not affect the conclusion of our paper. We have used a simple power-law spectrum of injected electrons in the radio components, and showed that, after time evolution, the total multiwavelength SED of the radio components cannot explain the X-ray and the gamma-ray data. Even if we assume a log-parabolic distribution for the injected electrons in the radio components, the time-evolved electron spectra cannot explain the high-energy radiation in X-ray and gamma-ray frequencies. The size and the age of each component and the Doppler factor of the jet frame were taken from M. Giroletti et al. (2005). The apparent velocities of the components are negligible compared to the jet velocity, so we utilized the Doppler factor of the jet frame to calculate the SEDs from the components. The Doppler factor depends on the jet orientation angle ( $\theta$ ), which is between  $2^\circ$

and  $4^\circ$  for the jet pointing toward us (M. Giroletti et al. 2005), and about  $177^\circ$  for the jet pointing away from us. The Doppler factor ( $\delta$ ), Lorentz factor ( $\Gamma$ ), intrinsic velocity ( $\beta$ ), and jet orientation angle ( $\theta$ ) are related by the following equation:

$$\delta = \frac{1}{\Gamma(1 - \beta \cos \theta)}. \quad (3)$$

With  $\Gamma = 1.5$ ,  $\beta = 0.76$ , and the Doppler factor  $\delta = 2.7$  for the jet with the N components, as given in M. Giroletti et al. (2005), and  $\delta = 0.38$  for the jet with the S components.

We have assumed that the electrons are accelerated by the first-order Fermi mechanism, and hence their spectral index is close to  $-2$ . The normalization of the electron spectrum is related to the jet power in electrons. The radio data points constrain the magnetic field and the normalization. The values of the parameters are presented in Table 1. In this way, we estimate the electron spectrum and magnetic field inside each component and subsequently evolve the electron spectrum to the current age of each component, to obtain the SED at the present epoch. The jet power required in the injected electrons is of the order of  $10^{40} \text{ erg s}^{-1}$  in N2 and N3, and  $10^{43} \text{ erg s}^{-1}$  in S1 and S2, respectively, and the magnetic field inside the radio components is lower than 1 mG. If we increase the maximum energies of the electrons in the N2 and N3 components, then we cannot fit the Swift X-ray data points after adding the SEDs of all the components, and if we increase the maximum energies of the electrons in the S1 and S2 components, then their SSC emissions become too high and the total SED exceeds the Fermi-LAT upper limits. Thus, the maximum energies of the electrons in the radio components are constrained by the X-ray data points and the Fermi-LAT upper limits. The radio data points' energies constrain the electrons' minimum energies in the radio components. Figure 3 shows the sum of the SEDs of the radio components at the present epoch, which cannot explain the Swift X-ray (Z.-R. Wang et al. 2024) and LHAASO gamma-ray data (Z. Cao 2024a). The SSC emissions from the S1 and S2 components may contribute to the gamma-ray spectrum near 100 MeV. In future, with the

detection of gamma rays by the Fermi-LAT detector, it will be possible to constrain the maximum energies of the electrons in the S1 and S2 components. Moreover, the double-hump structure in the SED of NGC 4278 disappears if the S1 and S2 components emit gamma rays near 100 MeV.

We have proposed that an additional component is required to explain the high-energy emission data obtained from Swift-XRT in photon-counting (PC) mode (Z.-R. Wang et al. 2024) and LHAASO (Z. Cao 2024a). Parameters such as the normalization of the injected electron spectrum and magnetic field inside the component have been varied to fit the high-energy data. The spectral index is chosen to be  $-2$ , as before. The minimum and maximum energy of the injected electrons are assumed to be higher than those of the radio components to produce very-high-energy secondary photons. The age of the component is assumed to be 30 yr, which is comparable to the age of the youngest radio component, N3. The Doppler factor of the comoving frame is 2.7, which is provided by M. Giroletti et al. (2005). The size of the high-energy component is assumed to be much smaller (0.005 pc) compared to the size of the radio components, so the SSC component is significantly higher and reaches the flux measured by LHAASO.

The values of the various parameters used in our modeling have been listed in Table 2. We have evolved the electron spectrum to obtain the SED at the present epoch, as shown in Figure 4. The jet power in injected electrons has to be  $5 \times 10^{39}$  erg s $^{-1}$ , and the magnetic field inside the component 8 mG; these two parameters are constrained by the synchrotron and SSC emission, which explains the Swift-XRT and LHAASO data. The SED fits the Swift X-Ray data (Z.-R. Wang et al. 2024), it is below the Fermi-LAT upper limits, and it also fits the LHAASO-WCDA measurements (Z. Cao 2024a). The total SED after adding all the components is shown in Figure 5.

## 5. Discussion

LLAGNs have been much less explored in comparison to high-luminosity AGNs. The time evolution of different emission components in the jets may play an important role in understanding this class of objects. The association of radio and X-ray flares with the knot ejection from M81\* (A. King et al. 2016) indicates a connection in the emission mechanisms of radio and X-ray photons. They are both produced in synchrotron emission of ultra-relativistic electrons (G. Tomar & N. Gupta 2023). In the case of NGC 4278 also, the radio and X-ray emission may be from synchrotron emission of ultra-relativistic electrons. However, in this case, we do not have simultaneous flare data in the radio and X-ray energy bands to show that the same population of electrons can explain the observed radio and X-ray data. Moreover, we see that the long-term data covering different frequency ranges cannot be explained with the same population of electrons; a separate emission region is required to explain the X-ray and gamma-ray observations. The gamma rays are produced in SSC emission in the model discussed in this work, which constrains the size of the emission region. In the case of M81\*, there are no gamma-ray data; only upper limits are available at present, which can only put a lower bound on the size of the emission region. The very-high-energy gamma-ray data recorded from the direction of NGC 4278 have been used here to constrain the size of the emission region, which has to be of the order of  $10^{16}$  cm to make the SSC bump high enough to reach the gamma-ray flux measured by LHAASO-WCDA.

The multiwavelength data from NGC 4278 were earlier modeled with leptonic and hadronic interactions by Z.-R. Wang et al. (2024). Their one-zone SSC model uses a steady-state, broken power-law electron density distribution as indicated in R. Xue et al. (2019). Their one-zone SSC model can fit the X-ray and very-high-energy gamma-ray data with extreme values of parameters. With an SSC +  $pp$  model considering a steady-state proton energy density, their SED fits all the data without requiring any extreme values of parameters. The sizes of the emission regions in their SSC models are  $8.5 \times 10^{13}$  cm and  $1.5 \times 10^{14}$  cm. The sizes of the emission regions in their SSC +  $pp$  models are  $10^{15}$  cm and  $3 \times 10^{15}$  cm. The internal optical depth of very-high-energy gamma rays depends on the density of the low-energy photons, which absorb the very-high-energy gamma rays. They have shown in their figures that the absorption of very-high-energy gamma rays by the low-energy photons inside the jet is not important for NGC 4278. In our modeling, the size of the high-energy emission region ( $1.5 \times 10^{16}$  cm) is larger than theirs, hence the internal optical depth does not attenuate the very-high-energy gamma-ray flux significantly. Moreover, due to the proximity of NGC 4278, its very-high-energy gamma-ray flux is not attenuated by the extragalactic background light. In our model, the magnetic field is lower than Z.-R. Wang et al.'s (2024), but the minimum and maximum energy of electrons are much higher at injection inside the high-energy component. These electrons have lost energy over 30 yr; their time-evolved spectrum has been used to calculate the radiation spectrum. In their work, the escape timescale of electrons is  $R/c$ , which is 10 times lower than the value used in our work. Since the electrons are escaping faster and they have used a steady-state electron spectrum to fit the high-energy observations, the luminosity in the injected electrons is higher in their paper. The value of the Doppler factor used in Z.-R. Wang et al. (2024) for the small viewing angle is similar to the value used in our work.

The emission from the host galaxy of NGC 4278 is shown by the archival optical data points in our figures, which is also present in other LLAGNs, e.g., NGC 315, NGC 1275 (G. Tomar et al. 2021), and M81\* (G. Tomar & N. Gupta 2023). Multiwavelength variability has been observed in these sources. The variability of M81\* in radio and X-ray frequencies has been modeled in G. Tomar & N. Gupta (2023); NGC 4278 also has variability in different frequencies (G. Younes et al. 2010; J.-S. Lian et al. 2024). However, a variability study is not the objective of this work. The latest LHAASO data points from Z. Cao (2024a) have been included in our figures to compare with the simulated spectrum. The light curve of NGC 4278 shows a variability timescale of a few months in TeV energy. A month-scale variability implies that the region size has to be less than  $R \leq 2 \times 10^{17}$  cm, which is consistent with the size of the emission region,  $1.5 \times 10^{16}$  cm, used in our work. The magnetic field of the high-energy emission region is estimated to be more than 5 mG in Z. Cao (2024b), which is consistent with the value of 8 mG used in our work.

Our study does not include the time evolution of the parameters of the components. The sizes of the components given in Table 2 of M. Giroletti et al. (2005) do not scale with their distances from the center of the S-shaped twin jets, hence it is not possible to use a conical geometry for the time evolution of the components. If the high-energy component is much younger than the youngest radio component, N3, then a smaller size would be required to enhance the SSC emission to

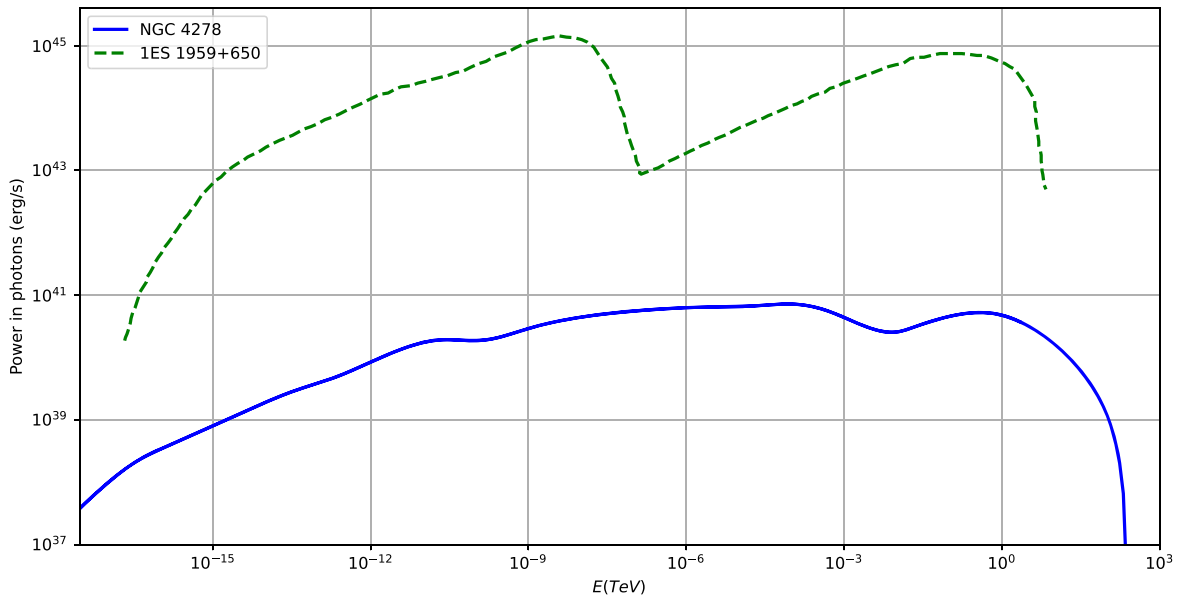


**Figure 6.** A comparison of the powers emitted in photons of NGC 4278 (from this paper) and 1ES 1959+650 during its intermediate state (MAGIC Collaboration et al. 2020).

explain the LHAASO data points. If the high-energy component is older than 30 yr, then the high-energy SED does not change significantly with time, hence it would be possible to fit the gamma-ray data for the same size high-energy component. The high-energy component must have electrons of much higher energy compared to the radio components, otherwise the very-high-energy gamma rays could not be produced in the jet of NGC 4278. It is unknown what may cause the high-energy component to be different from the radio components. If the acceleration of electrons is more efficient in the vicinity of the high-energy component, then there could be an injection of much more energetic electrons, which might produce the high-energy radiation by energy dissipation. Diffusive shock acceleration may become more efficient in turbulent reconnection, which is produced by large-amplitude magnetic disturbances in shocks (C. Garrel et al. 2018). In some cases, multiple zones or components are required to explain the multiwavelength data of blazars (R.-Y. Liu et al. 2023) in both low and high states. Substructures and bright knots have been observed along the jets of several blazars. The VLBA image of the M87 jet shows many substructures with different proper motions (F. Mertens et al. 2016). Simultaneous radio, optical, X-ray, and gamma-ray observations of 3C 279 revealed multiple energy dissipation regions in its jet (B. Rani et al. 2018). In several blazars, the flux variability in different energy bands cannot be correlated (MAGIC Collaboration et al. 2021), and in some cases, orphan gamma-ray flares have been observed (I. Lioudakis et al. 2019; MAGIC Collaboration et al. 2019; S. R. Patel et al. 2021). These results suggest there are multiple emission regions. Hence, different components in the jets of NGC 4278 indicate that LLAGNs may have multiple energy dissipation regions, similar to high-luminosity AGNs.

### 5.1. Comparison of NGC 4278 with Highly Peaked BL Lac Objects

MAGIC Collaboration et al. (2020) fitted the broadband spectra of five very-high-energy BL Lac objects with one-zone

and two-zone models. The MAGIC gamma-ray telescope detected TeV gamma rays from these sources; further, variability of these sources was detected in different energy bands, which helped the authors to model these sources. The one-zone model cannot fit the radio data though it can fit the optical to very-high-energy gamma-ray data. A larger emission region is required to fit the radio data compared to the data at higher frequencies. For NGC 4278 also, the radio components are larger compared to the high-energy component, and multiple components are required to fit the observational data covering the radio to very-high-energy gamma-ray frequencies. We compare the SED of NGC 4278 to the SED of the high-energy peaked BL Lac object 1ES 1959+650 during its intermediate state in Figure 6 as both emit very-high-energy gamma rays. The double-hump structure cannot be seen in the SED of NGC 4278 if the S1 and S2 components emit significantly near 100 MeV energy. The Doppler factors of NGC 4278 and 1ES 1959+650 differ by a factor of approximately 10, and the powers emitted in photons near 1 TeV gamma-ray energy differ by approximately a factor of  $10^4$ . Higher variability is expected in high-energy BL Lac objects due to the higher values of the Doppler factors. We notice that NGC 4278 resembles high-energy peaked BL Lac objects to some extent, although it is less luminous and has a slow jet.

## 6. Conclusion

We conclude that our model fits the archival radio data, fits the X-ray data of Swift analyzed by Z.-R. Wang et al. (2024), and fits the very-high-energy gamma-ray data of LHAASO (Z. Cao et al. 2024b) after adding the photon fluxes from multiple components as shown in Figure 5. We have shown that the radio components S1, S2, N3, and N2 cannot explain the Swift-XRT observations in the X-ray energy band and the high-energy gamma-ray data recorded by the LHAASO detector with their time-evolved electron spectrum. The S1 and S2 components may contribute to the gamma-ray spectrum near 100 MeV, which could be verified in future with Fermi-LAT data. A separate component is needed in the jet to model



the Swift-XRT and LHAASO data points. Simultaneous radio, X-ray, and gamma-ray observations are needed to study the individual components in the jets of NGC 4278 and other LLAGNs. Since they are closer to us, it would be easier to monitor the individual jet components over many years to understand the underlying mechanisms of jet emission. We note that NGC 4278 has characteristics similar to some high-luminosity AGNs, having multiple emission regions and radio components the sizes of which are larger than the size of the high-energy component.

### Acknowledgments

The authors thank the referee for helpful comments. They also thank Sovan Boxi for technical support related to software issues, Gunjan Tomar for helpful discussion, and K. S. Dwarakanath for explaining the error analysis of radio flux measurement. This research has made use of the NASA/IPAC Extragalactic Database (NED), which is operated by the Jet Propulsion Laboratory, California Institute of Technology, under contract with the National Aeronautics and Space Administration. S.D. thanks BITS, Pilani for local hospitality, where a part of this work was carried out.

*Software:* GAMERA (<http://libgamera.github.io/GAMERA/docs/documentation.html>).

### ORCID iDs

Samik Dutta  <https://orcid.org/0009-0005-6429-1921>

Nayantara Gupta  <https://orcid.org/0000-0002-1188-7503>

### References

- Baldini, L., Ballet, J., Bastieri, D., et al. 2021, *ApJS*, 256, 13  
 Bulgarelli, A., Fioretti, V., Parmiggiani, N., et al. 2019, *A&A*, 627, A13  
 Cao, Z., Aharonian, F., Axikegu, Y. X., et al. 2024a, *ApJL*, 971, L45  
 Cao, Z., Aharonian, F., An, Q., et al. 2024b, *ApJS*, 271, 25  
 Chiaberge, M., Sparks, W., Macchetto, F. D., et al. 2005, *ApJ*, 629, 100  
 de Menezes, R., Nemmen, R., Finke, J. D., Almeida, I., & Rani, B. 2020, *MNRAS*, 492, 4120  
 Garrel, C., Vlahos, L., Isliker, H., & Pisokas, T. 2018, *MNRAS*, 478, 2976  
 Giovannini, G., Cotton, W. D., Feretti, L., Lara, L., & Venturi, T. 2001, *ApJ*, 552, 508  
 Giroletti, M., Taylor, G. B., & Giovannini, G. 2005, *ApJ*, 622, 178  
 Hahn, J., Romoli, C., & Breuhaus, M. 2022, *ascl:2203.007*  
 Hartman, R. C., Bertsch, D. L., Bloom, S. D., et al. 1999, *ApJS*, 123, 79  
 Heckman, T. M. 1980, *A&A*, 87, 152  
 Ho, L. C. 2008, *ARA&A*, 46, 475  
 Ho, L. C., Filippenko, A. V., & Sargent, W. L. W. 1997a, *ApJ*, 487, 568  
 Ho, L. C., Filippenko, A. V., & Sargent, W. L. W. 1997b, *ApJS*, 112, 315  
 King, A., Miller, J., Bietenholz, M., et al. 2016, *NatPh*, 12, 772  
 Lian, J.-S., Li, J.-X., Hu, X.-K., et al. 2024, *arXiv:2405.00347*  
 Liodakis, I., Romani, R. W., Filippenko, A. V., Kocevski, D., & Zheng, W. 2019, *ApJ*, 880, 32  
 Liu, R.-Y., Xue, R., Wang, Z.-R., Tan, H.-B., & Böttcher, M. 2023, *MNRAS*, 526, 5054  
 MAGIC Collaboration, Acciari, V. A., Ansoldi, S., et al. 2019, *A&A*, 623, A175  
 MAGIC Collaboration, Acciari, V. A., Ansoldi, S., et al. 2020, *A&A*, 640, A132  
 MAGIC Collaboration, Acciari, V. A., Ansoldi, S., et al. 2021, *A&A*, 655, A89  
 Márquez, I., Masegosa, J., González-Martin, O., et al. 2017, *FRASS*, 4  
 Mertens, F., Lobanov, A. P., Walker, R. C., & Hardee, P. E. 2016, *A&A*, 595, A54  
 Narayan, R., & Yi, I. 1994, *ApJL*, 428, L13  
 Nemmen, R. S., & Brotherton, M. S. 2010, *MNRAS*, 408, 1598  
 Nemmen, R. S., Storchi-Bergmann, T., & Eracleous, M. 2014, *MNRAS*, 438, 2804  
 Netzer, H. 2015, *ARA&A*, 53, 365  
 Patel, S. R., Bose, D., Gupta, N., & Zuberi, M. 2021, *JHEAp*, 29, 31  
 Peck, A. B., & Taylor, G. B. 2000, *ApJ*, 534, 90  
 Rani, B., Jorstad, S. G., Marscher, A. P., et al. 2018, *ApJ*, 858, 80  
 Terashima, Y., Ho, L. C., & Ptak, A. F. 2000, *ApJ*, 539, 161  
 Tomar, G., & Gupta, N. 2023, *ApJ*, 950, 113  
 Tomar, G., Gupta, N., & Prince, R. 2021, *ApJ*, 919, 137  
 Tonry, J. L., Dressler, A., Blakeslee, J. P., et al. 2001, *ApJ*, 546, 681  
 Voges, W., Aschenbach, B., Boller, T., et al. 1999, *A&A*, 349, 389  
 Wang, T.-G., & Zhang, X.-G. 2003, *MNRAS*, 340, 793  
 Wang, Z.-R., Xue, R., Xiong, D., et al. 2024, *ApJS*, 271, 10  
 White, N. E., Giommi, P., & Angelini, L. 2000, *yCat*  
 Xue, R., Liu, R.-Y., Petropoulou, M., et al. 2019, *ApJ*, 886, 23  
 Younes, G., Porquet, D., Sabra, B., et al. 2010, *A&A*, 517, A33